ACS PHYSICAL CHEMISTRY Au
AN OPEN ACCESS JOURNAL OF THE AMERICAN CHEMICAL SOCIETY

pubs.acs.org/physchemau

Article

Ethanol and Water Adsorption in Conventional and Hierarchical All-Silica MFI Zeolites

Swagata Pahari,[#] Matheus Dorneles de Mello,[#] Mansi S. Shah, Tyler R. Josephson, Limin Ren, Huong Giang T. Nguyen, Roger D. Van Zee, Michael Tsapatsis, and J. Ilja Siepmann*

Cite This: *ACS Phys. Chem Au* 2022, 2, 79–88

Read Online

ACCESS | Metrics & More | Article Recommendations | Supporting Information

ABSTRACT: Hierarchical zeolites containing both micro- (<2 nm) and mesopores (2–50 nm) have gained increasing attention in recent years because they combine the intrinsic properties of conventional zeolites with enhanced mass transport rates due to the presence of mesopores. The structure of the hierarchical self-pillared pentasil (SPP) zeolite is of interest because all-silica SPP consists of orthogonally intergrown single-unit-cell MFI nanosheets and contains hydrophilic surface silanol groups on the mesopore surface while its micropores are nominally hydrophobic. Therefore, the distribution of adsorbed polar molecules, like water and ethanol, in the meso- and micropores is of fundamental interest. Here, molecular simulation and experiment are used to investigate the adsorption of water and ethanol on SPP. Vapor-phase single-component adsorption shows that water occupies preferentially the mesopore corner and surface regions of the SPP material at lower pressures (P/P_0 < 0.5) while loading in the mesopore interior dominates adsorption at higher pressures. In contrast, ethanol does not exhibit a marked preference for micro- or mesopores at low pressures. Liquid-phase adsorption from binary water–ethanol mixtures demonstrates a 2 orders of magnitude lower ethanol/water selectivity for the SPP material compared to bulk MFI. For very dilute aqueous solutions of ethanol, the ethanol molecules are mostly adsorbed inside the SPP micropore region due to stronger dispersion interactions and the competition from water for the surface silanols. At high ethanol concentrations (C_{EtOH} > 700 g L^{-1}), the SPP material becomes selective for water over ethanol.

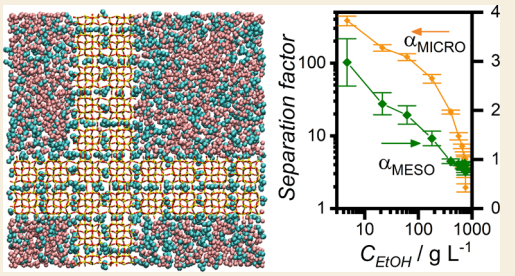

KEYWORDS: *Vapor Adsorption, Liquid Adsorption, Micro/Mesoporous Materials, Monte Carlo Simulation, Adsorption Selectivity, Sorbate Siting*

1. INTRODUCTION

Zeolites are crystalline inorganic porous materials formed by corner-sharing TO_4 tetrahedra (with T being Si, Al, or other heteroatoms).[1] Zeolites have ordered micropores (with pore diameters between 0.5 to 2 nm), which confer them important properties in industrial applications, such as catalysis[2−4] and separations.[5−8] However, significant mass transfer limitations to bulkier molecules, often present in oil and biomass processing, exist for microporous zeolites and lead to challenges for certain applications.[9,10]

The synthesis of hierarchical zeolites, materials that combine zeolitic micropores with a mesoporous network, has been motivated as a way to enhance mass transfer rates while preserving desirable features of the micropores for catalysis and separation applications.[11−16] As limiting cases, single-unit-cell hierarchical zeolites like pillared MWW and MFI were developed containing a mesoporous gallery structure along with sheets possessing the characteristic micropores of these materials.[17,18] Our group reported the synthesis of the intergrowth of MFI/MEL in a house-of-cards morphology, known as self-pillared pentasil (SPP) zeolite.[19] The SPP material consists mostly of single-unit-cell MFI nanosheets orthogonally intergrown to each other with MEL present at the branching points. Along with enhanced transport properties, such materials have interesting properties for catalysis applications.[20−22] An important aspect of the SPP hierarchical structure is that its mesopores exhibit a Si−OH rich hydrophilic surface (terminated by silanol groups on the external surfaces of the nanosheets), which can synergistically contribute to catalysis, as was suggested by Josephson and co-workers[23,24] and other groups for related systems.[25−27]

A less explored and particularly exciting aspect of the SPP material is that it provides hydrophobic and hydrophilic regions, that are in nanometer scale proximity, for adsorption or chemical transformations of molecules that have different degrees of affinity to silanol groups and hydrophobic pores. Here we attempt to assess the distribution of adsorbed water and ethanol molecules in SPP. Since we cannot experimentally obtain the distribution of molecules in the different domains,

Received: September 2, 2021
Revised: October 21, 2021
Accepted: October 22, 2021
Published: November 17, 2021

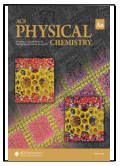

https://doi.org/10.1021/acsphyschemau.1c00026
ACS Phys. Chem Au 2022, 2, 79–88

we assess it by a combination of molecular simulations validated by experimental isotherms. Ultimately, we demonstrate that it is possible to segregate molecules of different polarity in distinct spaces with nm proximity.

2. MATERIALS AND METHODS

2.1. Adsorbent Synthesis

Samples of hydrophobic, all-silica MFI zeolite synthesized by the fluoride method,[28] referred herein as MFI-F, and of all-silica SPP[19] were taken from prior work. These references also provide details of the materials characterization.

2.2. Vapor-Phase Adsorption Experiments

Water and ethanol unary sorption isotherms were measured at 298 K. The experiments were conducted on a TA Instruments VTI-SA+ vapor sorption analyzer located at the Facility for Adsorbent Characterization and Testing at the National Institute of Standards and Technology. (Commercial equipment is identified in the paper in order to specify the experimental procedure adequately. This identification is not intended to imply recommendation by NIST nor is it intended to imply that the equipment identified are necessarily the best available for the purpose.) The instrument is a dynamic vapor sorption system that obtains the desired relative humidity or partial pressure value by continuously mixing dry nitrogen flow with a humid nitrogen flow. The zeolite sample (25 mg) was activated in situ at 413 K for up to 8 h under a constant flow of pure nitrogen before starting each experiment.

2.3. Liquid-Phase Adsorption Experiments

Batch-adsorption experiments were conducted at 323 ± 0.5 K. The alcohol solution to adsorbent mass was varied from 4 to 8 mL/g. Approximately 100 mg of zeolite with an appropriate amount of ethanol/water solution was added to glass vials (C4011-1, crimp seal, Thermo Scientific). Then the vials were rotated at 20 rpm in a ProBlot12 hybridization oven until equilibrium was reached. The supernatant solutions were filtered using a Monoject syringe fitted with a 0.2 μm hydrophilic polypropylene (GHP) syringe filter to remove the zeolite particles.

Solution concentrations were analyzed with an Agilent 7890B gas chromatograph equipped with a fused silica column (Rtx-VMS, Restek) and a flame ionization detector. The relative signal intensities of the adsorbate and a 1-butanol (99.5%, Aldrich) internal standard were used to determine the concentrations. A coadsorption approach as suggested by DeJaco et al.[29] was used to determine the water and ethanol loadings. The coadsorption approach relies on information from molecular simulation to circumvent the assumptions (e.g., no solvent adsorption) that otherwise must be used to close the mass balance. This molecular-level information is important for the SPP material because water, as the solvent, is found to fill the mesopores but not the micropores. Thus, using one of the common assumptions (e.g., no-solvent adsorption or filling of the entire pore volume by solvent) would lead to erroneous loading data. Further details on the coadsorption model are provided in the Supporting Information.

2.4. Molecular Simulation Details

The structure of all-silica MFI for the simulation was taken from the work of van Koningsveld et al.,[30] where the simulation box consists of a 2 × 2 × 3 supercell of MFI with the length in the *x*-, *y*-, and *z*-axis being 40.044, 39.798, and 40.149 Å, respectively. The structure of the SPP zeolite was constructed starting from a 4 × 4 × 3 supercell of MFI with the length in the *x*-, *y*-, and *z*-axis being 80.088, 79.596, and 40.149 Å, respectively. To generate a mesopore,[31,32] a section of the supercell material was removed by cutting between the polar chains (perpendicular to the *b*-direction) and between pentasil layers (perpendicular to the *a*-direction) and, subsequently, saturating each terminal oxygen atom with a hydrogen atom to form surface silanol groups. Here, we used the SPP-C model[31] that contains single-unit cell MFI sheets with a thickness of 20 Å yielding a mesopore cross section and volume fraction of 60 Å and 0.55, respectively. The SPP structure is illustrated in Figure 1. We further divided the SPP mesopore into three regions: (i) the (external) surface region of the

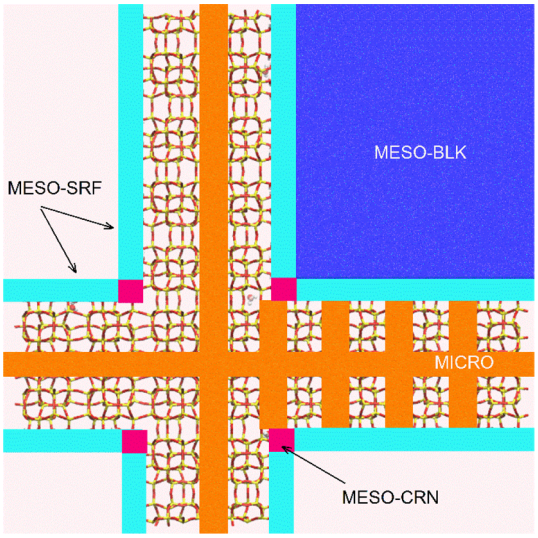

Figure 1. *xy*-Projection of the SPP-C structure identifying the four SPP regions (MICRO, MESO-SRF, MESO-CRN, and MESO-BLK) used to assess adsorbate distribution.

nanosheets, which consists of the (100) and (010) faces of MFI (called MESO-SRF, that was assigned here a thickness of 4 Å from the terminal oxygen atoms of the Si−OH groups to reflect the small size and strong localization due to hydrogen bonding of the water and ethanol adsorbates, whereas a larger thickness was used previously for analysis of alkane and furan adsorption[24,31]); (ii) the corner region near the intersection of two orthogonal nanosheets (called MESO-CRN, with a cross-section of 4 by 4 Å); and (iii) the mesopore interior region (called MESO-BLK).

The sorbent−sorbate and sorbate−sorbate intermolecular interactions were described through a combination of Lennard−Jones (LJ) 12-6 and Coulomb potentials. The TIP4P model[33] was used for water molecules. For alcohol molecules and zeolite adsorbents, the parameters were taken from the Transferable Potentials for Phase Equilibria (TraPPE) force field.[34−36] Here, the LJ parameters for silanol hydroxyl groups, bending, and torsional potentials of silanol hydrogens were taken from the TraPPE force field for alcohols. The partial charges for (interior) silicon and oxygen atoms in zeolites are +1.50 |e| and −0.75 |e|. Following previous simulations for chromatographic systems,[37] the charge of the silanol hydrogen atom was set to +0.435 |e|, which is the same as that of the TraPPE alcohol model, the charge on the silanol oxygen atom was set to −0.739 |e|, and the charge on the silanol silicon atom was adjusted from the TraPPE-zeo value to maintain charge neutrality. The LJ parameters for unlike interactions were obtained using Lorentz−Berthelot combining rules. For LJ interactions, a spherical potential truncation was used at a distance of 14 Å and analytical tail corrections were used to estimate LJ interactions beyond this distance.[34−36] Coulomb interactions were treated using the Ewald summation method.[38] The host−guest interactions for the rigid portion of the zeolite framework (except surface silanol groups) were pretabulated using a grid spacing of 0.1 Å and interpolated during simulations.[36]

Dual cutoff, coupled-decoupled configurational-bias Monte Carlo (MC) simulations[39,40] in the isobaric−isothermal version of the Gibbs ensemble[41,42] were performed to obtain unary vapor-phase adsorption isotherms for water and ethanol at T = 298 K over a range of reduced pressures from 0.0035 to 0.97 as well as binary liquid-phase adsorption isotherms for water/ethanol mixtures at T = 323 K and P = 1 bar = 0.1 MPa. For the unary adsorption, two simulation boxes representing the zeolite and vapor phases were used and the system size consisted of 6000 water or ethanol molecules that can be

https://doi.org/10.1021/acsphyschemau.1c00026
ACS Phys. Chem Au 2022, 2, 79−88

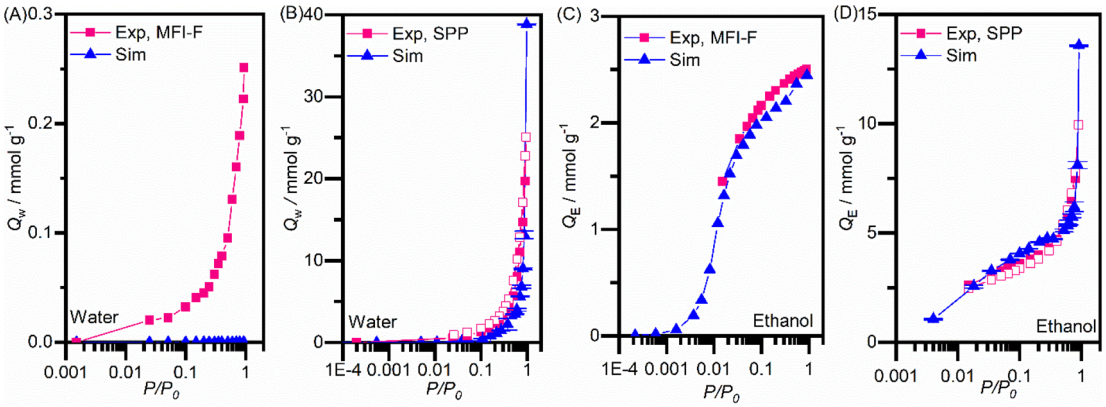

Figure 2. Vapor-phase water and ethanol adsorption in MFI-F and SPP at 298 K: (A) water in MFI-F; (B) water in SPP; (C) ethanol in MFI-F; and (D) ethanol in SPP. Filled and open symbols refer to adsorption and desorption branches, respectively. The adsorption data in MFI-F are taken from DeJaco et al.[29] Uncertainties are determined from four independent simulations. Note the different scales in adsorption capacities of water and ethanol for MFI-F and SPP. Lines are drawn only to guide the eye and do not reflect a fit to an adsorption isotherm function. Error bars show standard deviations obtained from four independent simulations. Numerical values are reported in the SI.

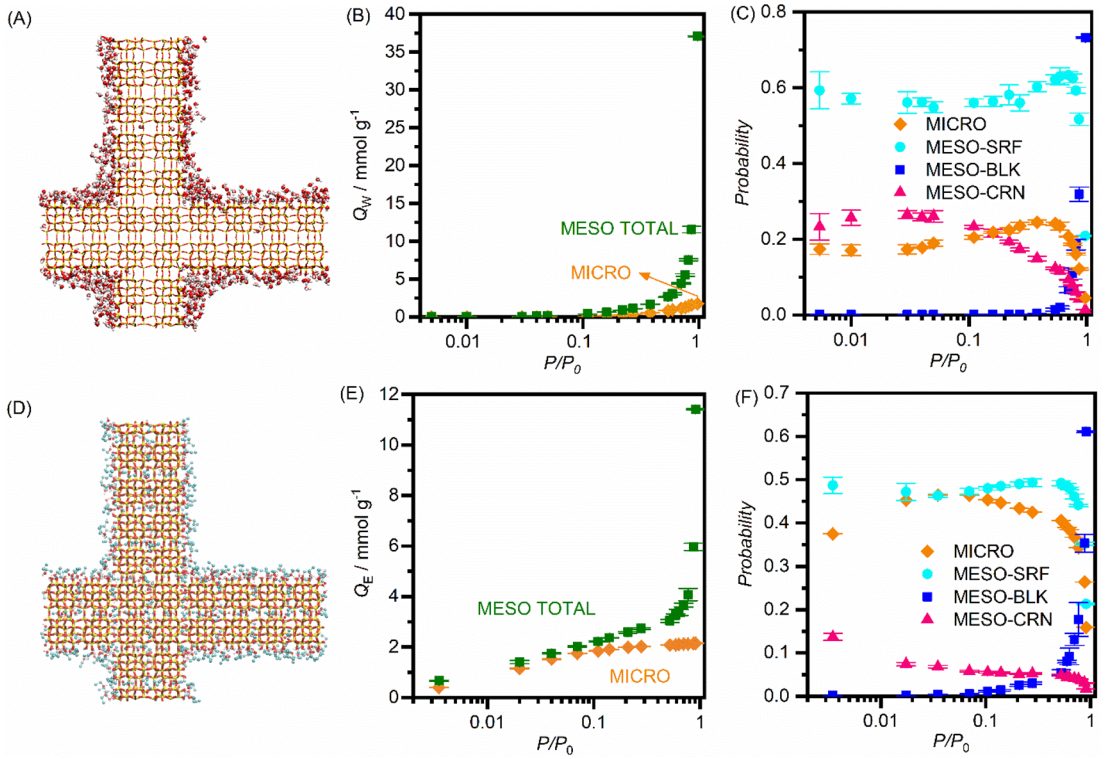

Figure 3. Simulation snapshots illustrating the loading of water (A) and ethanol (D) in SPP at P/P_0 = 0.38 and 0.28, respectively; oxygen, hydrogen, and CH_x (pseudo-)atoms of sorbate molecules are shown as red, gray, and cyan spheres, respectively, and the SPP structure is represented as wire frame. Water (B) and ethanol (E) loading in the micropore region (orange) and all mesopore regions (green). Probability of adsorption of water (C) and ethanol (F) in the micropore (orange), mesopore surface (cyan), mesopore interior (blue), and mesopore corner (magenta) regions. Error bars show standard deviations obtained from four independent simulations. Numerical values are reported in the SI.

transferred between the phases. For solution-phase adsorption, three simulation boxes were used representing the zeolite, solution phase, and vapor phase transfer medium. The simulated system consisted of approximately a total of 6000 water and ethanol molecules, and 12 water/ethanol ratios ranging from $2^6/1$ to $1/2^5$ (note that due to preferential adsorption, the equilibrium composition for the solution phase does not follow the powers of 2). Each adsorption simulation was initialized with an empty zeolite box (i.e., reflects the adsorption branch for cases with adsorption hysteresis). Equilibration and production periods of 300 000 MC cycles and 100 000 MC cycles were performed, respectively, where a cycle consists of N randomly selected MC moves (where N is the number of adsorbate molecules). The move types included translations and rotations of water and ethanol molecules, conformational changes for ethanol molecules and silanol groups (whereas all the other framework atoms remained at their crystallographically determined positions), water and ethanol transfer moves between the simulation boxes, and volume moves for the vapor- or solution-phase reservoirs. Four independent simulations were carried out at each state point, and statistical uncertainties are reported here as the standard deviations obtained from these independent simulations.

https://doi.org/10.1021/acsphyschemau.1c00026
ACS Phys. Chem Au 2022, 2, 79−88

3. RESULTS AND DISCUSSION

3.1. Unary, Vapor-Phase Adsorption

The vapor-phase adsorption isotherms for water and ethanol in MFI-F and SPP at 298 K are shown in Figure 2 (numerical values for adsorption in SPP are listed in Tables S1−S4 in the Supporting Information (SI)). The experimental data show very low water adsorption on MFI-F over the entire pressure range (Figure 2A), as expected for a nearly defect-free, hydrophobic material, and even lower loadings are observed for the perfect MFI framework considered for the simulations.[43] The aliphatic chain in ethanol allows for more favorable dispersion interactions with the hydrophobic MFI framework, leading to significant adsorption loading of about 1 mmol g^{-1} at $P/P_0 = 0.01$ and a saturation capacity of about 2.5 mmol g^{-1} with filled micropores at high P/P_0 (>0.9) (Figure 2C). The simulated and experimental ethanol isotherms in MFI-F show excellent agreement.

Both experiment and simulation (Figure 2B) show that the adsorption loading of water in SPP increases approximately linearly with pressure for $P/P_0 < 0.3$ but the loadings obtained from experiment exceed those from the simulations by a factor of about 2−3. Starting at $P/P_0 > 0.4$, the rate of the water uptake increases rapidly; the experimental data reach a loading of about 25 mmol g^{-1} at $P/P_0 = 0.94$, whereas the simulations predict a loading of about 39 mmol g^{-1} at $P/P_0 = 0.97$. Water adsorption on hydrophilic materials can yield significant variations due to imperfections in the crystals, which could include the presence of defects with silanol groups.[44−47] Our experimental isotherm shows higher uptakes than the simulated isotherms (about twice the predicted loading) between $0.1 < P/P_0 < 0.9$, which we attribute to the unavoidable presence of silanol defects in the MFI micropores when synthesis proceeds under typical basic conditions. The higher loading observed in the simulations near P_0 may reflect a larger mesopore volume fraction for the SPP-C model system than for the synthesized material.

Ethanol shows appreciable adsorption loadings on SPP at much lower P/P_0 (Figure 2D); for $P/P_0 < 0.01$, the ethanol loading exceeds that of water by more than an order of magnitude. At intermediate pressures, the simulation data fall slightly above the experimental value. At $P/P_0 = 0.90$, the experimental adsorption loading reaches 10 mmol g^{-1}, and simulations predict a loading of 13.6 mmol g^{-1} at $P/P_0 = 0.91$.

We further investigated the desorption of water and ethanol from SPP by experimental measurements (see Figure S1). Water can be removed entirely from the pores of SPP at room temperature as indicated by the matching adsorption−desorption isotherms obtained during the first and second cycles. As should be expected for a mesoporous material with a distribution of mesopore sizes, there is a small degree of hysteresis that extends down to $P/P_0 = 0.025$. The loading behavior for ethanol in SPP is more complex during multiple adsorption−desorption cycles. Slightly lower ethanol uptakes are observed in subsequent cycles, which could be an indication that small amounts of ethanol get trapped in the framework.

Analysis of simulation trajectories allows us to obtain additional information on the distribution of the adsorbate molecules in the hierarchical SPP material.[31] Snapshots taken from the water and ethanol adsorption simulations in SPP at $P/P_0 \approx 0.3$ (Figure 3A and D) indicate that water molecules avoid the hydrophobic micropores and occupy mostly the mesopore surface and corner regions where water molecules can form hydrogen bonds to surface silanols and also among each other. There is also a clear sign of multilayer water adsorption near the mesopore corner to reduce the curvature and surface area of the adsorbed water/vapor-like mesopore interior interface. In contrast, the ethanol molecules occupy uniformly the hydrophobic micropores in SPP and also sit on the mesopore surface and corner regions with their hydroxyl groups pointing toward the surface (to allow for hydrogen bonding) and their tail groups pointing away from the surface. Due to this orientation preference, multilayer adsorption of ethanol near the mesopore corner is not observed because additional ethanol molecules see mostly the tail groups and cannot form hydrogen bonds. The contributions from mesopores and micropores to water adsorption in SPP (Figure 3B, see also Table S1) indicate that adsorption in the micropores of the MFI nanosheets significantly exceeds that found for bulk MFI-F at the corresponding pressures but remains much below the saturation capacity in defect-free bulk MFI materials at much higher pressures.[36,44] The reason for the micropore loading of water is the formation of hydrogen-bonded fingers that extend from the pore mouth into the outermost region of the micropores (Figure 3A). However, even at $P/P_0 = 0.97$, the micropore adsorption in the nanosheets in not sufficient to lead to a percolating hydrogen-bonded network and the water loading in the mesopore regions exceeds that in the micropores by a factor of 20. Ethanol adsorption (Figure 3E, see also Table S2) is qualitatively different from water adsorption. Ethanol molecules adsorb on both micro- and mesopores at all pressures. The micropore region reaches a saturation loading of 2.2 mmol g^{-1}, which is comparable to the ethanol saturation loading in MFI-F of 2.5 mmol g^{-1} (refer to Figure 2C for comparison) when considering that, for a unit cell thick nanosheet, a fraction of the channels are now half-channels or grooves on the mesopore surface. When the relative pressure is increased from 0.52 to 0.91, the micropore loading increases only by 4%, whereas the mesopore loading increases by a factor of 3.8 as the mesopore interior is rapidly filled.

The fractions of water or ethanol molecules (Figure 3C and F, see also Tables S5 and S6) adsorbed in each particular region of the SPP material (Figure 1) are given here in the form of probabilities. For $P/P_0 < 0.1$, about 25, 56, and 18% of the water molecules are found to adsorb in the mesopore corner, mesopore surface, and micropore regions, respectively. However, when accounting for the fact that the volume of the surface region is about 13 times larger than that of the corner region, it is clear that water molecules preferentially adsorb in the mesopore corner region because they can form multiple hydrogen bonds with silanol groups. The corner regions are quickly saturated and their contribution to the overall loading decreases for $P/P_0 > 0.05$. The fractional loadings of water onto mesopore surface and micropore channels slightly increase for $P/P_0 > 0.05$ and reach values of 63 and 24%, respectively, at $P/P_0 \approx 0.6$. At this point, the loading in the mesopore interior takes off and crosses 50% at $P/P_0 \approx 0.9$. In contrast to the water distribution, adsorption in the micropore region contributes about 40% of the total ethanol loading for $P/P_0 < 0.5$ (Figure 3F). Accounting again for the differences in volume of the different regions, the initial adsorption at $P/P_0 = 0.0035$ favors the mesopore corner and micropore regions. The former is the best environment for hydrogen bonding to surface silanols, whereas the latter allows for favorable

https://doi.org/10.1021/acsphyschemau.1c00026
ACS Phys. Chem Au 2022, 2, 79−88

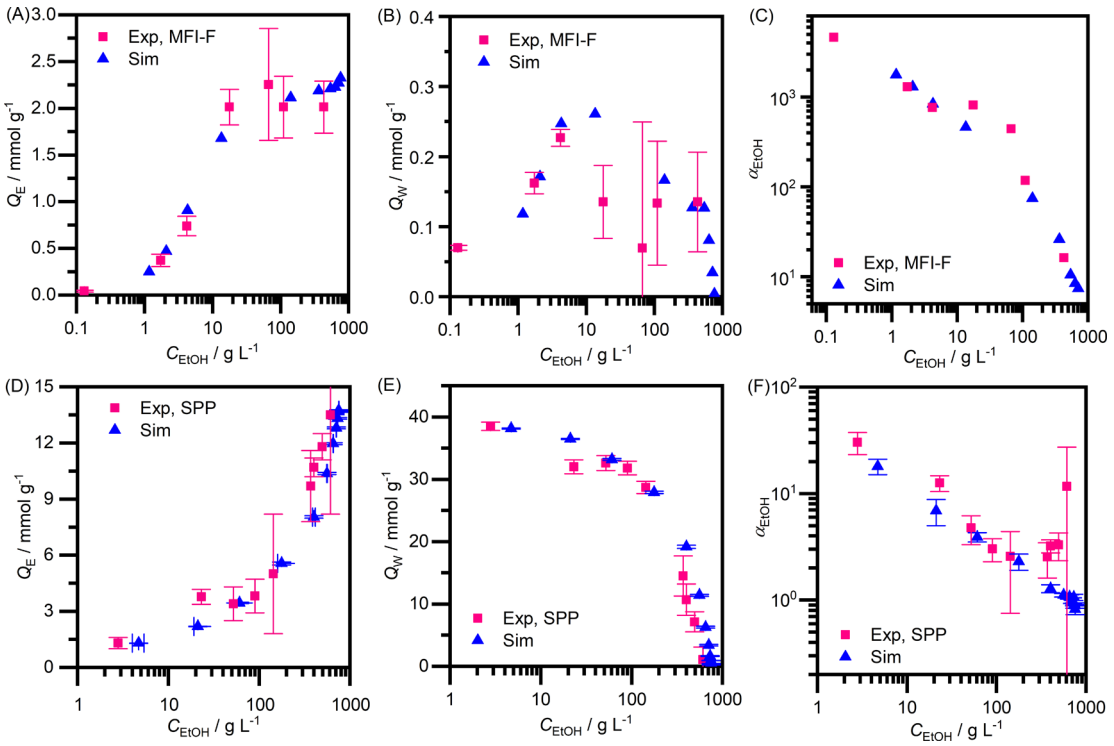

Figure 4. Ethanol loadings (left), water loadings (middle), and ethanol/water separation factors (right) for liquid-phase adsorption in MFI-F (A–C) and SPP (D–F) at 323 K as a function of the equilibrium concentration of the liquid solutions. The adsorption data in MFI-F are taken from DeJaco et al.[29] Uncertainties are determined from four independent simulations. Experimental uncertainties are determined from either replicate experiments or error propagation. Numerical values are reported in the SI.

dispersion interactions with the micropore channel walls. At intermediate pressures, the opportunity for ethanol–ethanol hydrogen bonding increases the loading fraction for the micropore channels. At $P/P_0 \approx 0.7$, the ethanol loading in the mesopore interior takes off and also crosses 50% at $P/P_0 \approx 0.9$.

3.2. Binary, Liquid-Phase Adsorption

Motivated by the profound differences in the loading preferences of water and ethanol found in the unary adsorption simulations, we now shift focus to the competitive adsorption of ethanol–water mixtures in SPP from liquid solution and again compare to prior experimental and simulation data for MFI-F.[19] As discussed by DeJaco et al.,[29] analysis of batch adsorption experiments from liquid solution requires one assumption to be made for solving the mass balance equations and determining the loading of all species (given the number of unknown variables and the number of mass balance equations). DeJaco et al.[29] observed that application of any of these assumptions can qualitatively impact the loading determined from the mass balance equations and proposed an approach using a combination of the predicted coadsorption by simulation coupled with the bulk solution concentrations measured, referred to as the coadsorption method. The method was applied to accurately determine the solute/solvent loadings for ethanol/water and pentan-1,5-diol/(water or ethanol) solutions coadsorbed in defect-free MFI. We used the coadsorption approach here to determine the adsorption loadings of ethanol and water from solution in SPP. Details of the calculations can be found in section S2.

The coadsorption relation between Q_E and Q_W for the SPP sorbent depicted in Figure S2 indicates that Q_W decreases approximately linearly as a function of Q_E for $Q_E > 5$ mmol g^{-1} but the decrease is sublinear for $Q_E < 5$ mmol g^{-1}. We fit the solvent loading using a combination of rapidly decreasing exponential and linear terms (see section S2). This relation accounts for the initial adsorption of ethanol in the hydrophobic SPP micropores without significant displacement of water, followed at higher concentrations by ethanol adsorption in the mesopores that require displacement of water (the linear region for $Q_E > 5$ mmol g^{-1}). This coadsorption behavior in SPP is different from that observed for a pentan-1,5-diol/ethanol mixture in MFI-F, where any adsorbed diol molecules must displace some solvent molecules to adsorb.[29]

Binary ethanol–water liquid-phase adsorption isotherms onto both MFI-F and SPP are presented in Figure 4 (and numerical data are provided in Tables S7–S10). Good agreement is observed between simulations and the experimental measurements analyzed with the coadsorption approach. The ethanol loading in MFI-F gradually increases to about 2.3 mmol g^{-1} at high ethanol concentrations (Figure 4A), in agreement with the unary vapor-phase adsorption data (Figure 2C). As the ethanol concentration increases, a small amount of water coadsorbs in the micropores, dropping to almost zero at high loadings (Figure 4B). All-silica MFI has been investigated for the adsorption of alcohols and polyols from aqueous solutions.[29,48−51] The micropores are selective for alcohols with small quantities of water coadsorbing.[48,52−54]

SPP shows a different behavior compared to MFI-F but bears similarities to adsorption on silicalite-1 films.[55] At low ethanol concentrations, the water loading in SPP is high due to adsorption in the mesopores with their hydrophilic surfaces (Figure 4). The simulations yield a water loading of 38 mmol g^{-1} for $C_{EtOH} = 5$ g L^{-1} in agreement with the unary adsorption data for $P \approx P_0$ (Figure 2B). For $C_{EtOH} < 100$ g L^{-1}, the

https://doi.org/10.1021/acsphyschemau.1c00026
ACS Phys. Chem Au 2022, 2, 79–88

ethanol loading in SPP increases steadily reaching a value of 4 mmol g^{-1} and the water loading decreases slowly to 33 mmol g^{-1}. At $C_{EtOH} \approx 100$ g L^{-1}, the plot as a function of logarithmic concentration exhibits a discontinuity in the slope and higher concentrations lead to a more rapid increase in Q_E and decrease in Q_W. The ethanol loading reaches 14 mmol g^{-1} as the ethanol concentration increases (Figure 4D), which is consistent with the unary adsorption data (Figure 2D).

The separation factors for ethanol over water (see section S3 for details of their calculation) highlight the pronounced differences in the selective adsorption of water and ethanol in hydrophobic MFI-F and the hierarchical SPP material with hydrophilic mesopores (Figure 4C and F). For $C_{EtOH} < 1$ g L^{-1}, the separation factor in MFI-F exceeds 1000, whereas extrapolation of the simulation and experimental data in SPP yields a separation factor of only ≈40 at $C_{EtOH} < 1$ g L^{-1}. At the intermediate concentration of $C_{EtOH} = 100$ g L^{-1}, the separation factor for adsorption onto MFI-F is still ≈100, whereas the separation factor in SPP deduced from the experimental data is close to 3 at that point and remains near this value also at higher concentrations. The molecular simulations yield $\alpha \approx 3$ and 1 at $C_{EtOH} \approx 100$ and 700 g L^{-1}, respectively. The microscopic reasons for the reversal in the separation factor are discussed below.

To probe the thermodynamics of ethanol and water adsorption onto SPP, the Gibbs free energies of adsorption are calculated following the approach discussed by Ben-Naim and Mazo,[56,57] that is, using the number density ratios for ethanol and water in the two phases (see section S3 for details). As illustrated in Figure 5 (numerical data are provided

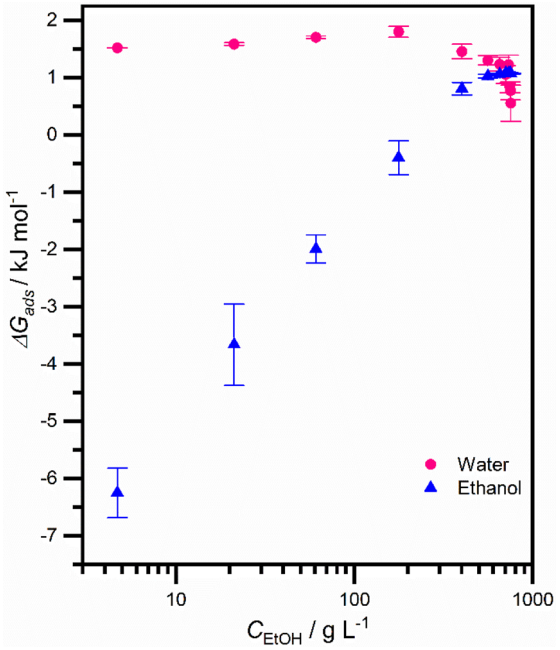

Figure 5. Gibbs free energies of adsorption for water and ethanol onto SPP at 323 K as a function of equilibrium solute concentration.

in Table S11), ΔG_{ads} for ethanol is most favorable at low ethanol concentrations with a value of −6.2 kJ mol^{-1} at $C_{EtOH} = 5$ g L^{-1}; that is, the SPP environment (particularly, the hydrophobic micropores) is preferred by ethanol over the aqueous solution phase presumably through a combination of the hydrophobic solvation penalty for the ethyl tail group and the strong dispersion interactions in the narrow micropores. As the solution-phase ethanol concentration increases, ΔG_{ads} for ethanol becomes less favorable. Again, two factors contribute to this change: aggregation of ethyl tails makes the solution phase more hospitable, and, once the micropores are filled by ethanol, additional adsorption in the mesopore leads to an unfavorable environment for the ethyl group. For $C_{EtOH} > 500$ g L^{-1}, ΔG_{ads} for ethanol reaches a plateau at +1.1 kJ mol^{-1}. While ΔG_{ads} for ethanol shows a strong concentration dependence, the changes for water are relatively minor and ΔG_{ads} is always positive (i.e., adsorption is unfavorable) throughout the entire concentration range. At $C_{EtOH} = 5$ g L^{-1}, ΔG_{ads} for water is +1.1 kJ mol^{-1} and initially increases slightly with increasing C_{EtOH} (reaching a value of +1.1 kJ mol^{-1} at $C_{EtOH} = 200$ g L^{-1}). At high C_{EtOH}, however, ΔG_{ads} for water decreases slightly to 0.6 kJ mol^{-1} as water adsorption can shift to the more favorable mesopore corner and surface sites.

The adsorption from binary ethanol−water solutions in different locations of SPP can be visualized by snapshots of equilibrated configurations for the zeolite phase (Figure 6A−C). At low ethanol concentration (5 g L^{-1}), ethanol occupies the micropores of SPP while water fills the mesopores. The concentration of ethanol in the mesopore region is very low, but the molar concentration of water in the micropore exceeds that of ethanol as water fingers extend into the micropore mouths. Water also partially occupies the interior micropore region at $C_{EtOH} = 5$ g L^{-1}, a concentration that is near the coadsorption maximum for MFI-F (Figure 4B). As the ethanol concentration increases to 400 g L^{-1}, ethanol and water compete for the surface and corners of the mesopores in SPP but ethanol still occupies the micropores and has nearly completely displaced the water molecules from the micropores, similar to the situation in MFI-F (Figure 4B). At high concentration (750 g L^{-1}), ethanol dominates the adsorption of both micro- and mesopore regions. The remaining water molecules are scattered in the different regions of the mesopore, surrounded by ethanol molecules.

A more quantitative representation of the distributions of water and ethanol obtained by averaging over the molecular simulation trajectories is presented in Figure 6D,E. At $C_{EtOH} = 5$ g L^{-1}, the ethanol loading in the micropores is already 1.1 mmol g^{-1} or about 50% of the micropore saturation loading (compare to Figure 3E for the unary vapor-phase adsorption). At this C_{EtOH}, the water loading is 1.5 mmol g^{-1}, a value that is more than 80% of the loading observed for unary vapor-phase adsorption near P_0 (Figure 3B). The water loading can reach this high value despite that about 50% of the micropore volume is filled by ethanol molecules because hydrogen bonding to ethanol molecules now allows water to also access the interior region of the micropore instead of mostly being confined to the pore mouth as in the unary adsorption. At $C_{EtOH} = 400$ g L^{-1}, the ethanol loading in the micropores has reached 2.1 mmol g^{-1} and the water loading has dropped by a factor of 5 to 0.3 mmol g^{-1}. Upon a further increase in C_{EtOH}, water is nearly completely displaced from the micropore region. For $C_{EtOH} < 100$ g L^{-1}, the ethanol loading in the mesopore region increases only slowly as a 12-fold increase in C_{EtOH} yields an 8-fold increase in the loading (Figure 6D); concomitantly, the water loading in the mesopores decreases by less than 20%. At higher concentrations, ethanol also displaces water from the mesopore region.

Figure 6E (Table S11) carries this analysis further by providing information on the probabilities of finding water and

https://doi.org/10.1021/acsphyschemau.1c00026
ACS Phys. Chem Au 2022, 2, 79−88

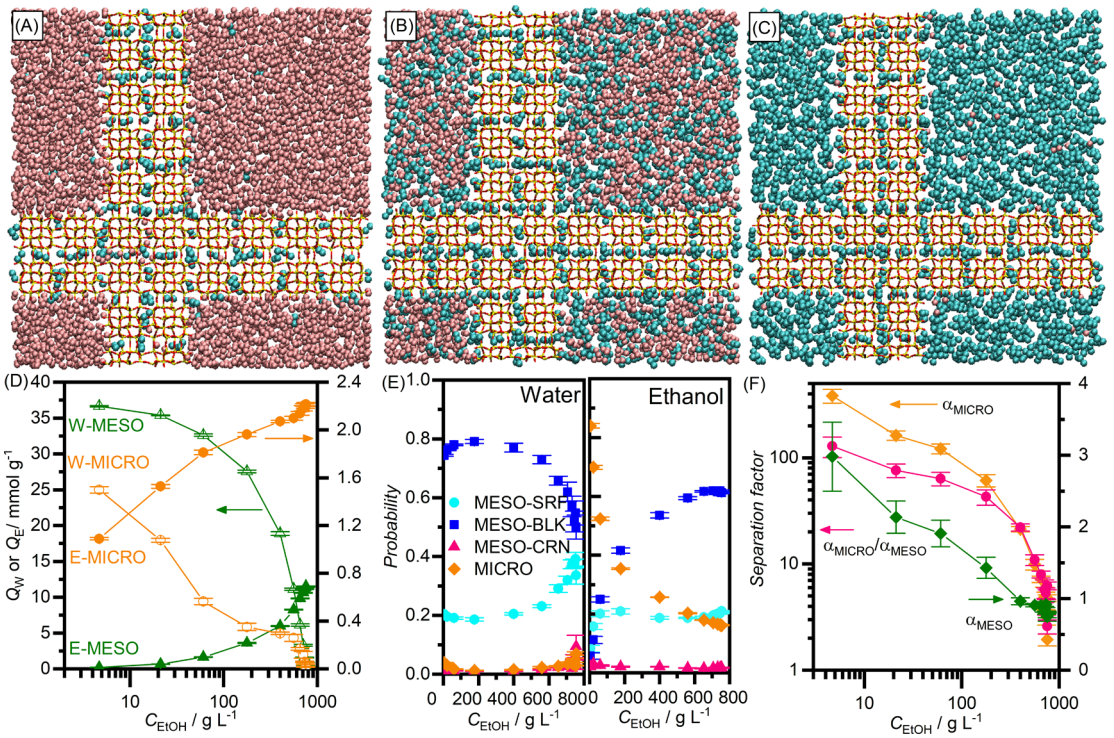

Figure 6. Snapshots of SPP loaded with ethanol and water at 323 K: (A) C_{EtOH} = 5 g L^{-1}, (B) C_{EtOH} = 400 g L^{-1}, and (C) C_{EtOH} = 752 g L^{-1}. (D) Contributions from micropores (orange, scale on right) and mesopores (green, scale on left) to the ethanol and water (closed and open symbols, respectively) adsorption onto SPP at different ethanol concentrations. (E) Probability of finding water and ethanol adsorbed on the four different SPP regions. (F) Ethanol/water separation factors in the micropore region (orange) and mesopore region (green) and the ratio of these separation factors (pink) as a function of ethanol concentration.

ethanol in the four distinct regions of the hierarchical SPP material (Figure 1). As C_{EtOH} increases, the distribution of ethanol over the four regions follows mostly monotonic trends; that is, the fraction of ethanol molecules found in the micropore region decreases from 84% to 16%, that in the mesopore interior increases from 6% to 62%, that on the mesopore surface increases from 8% to 21%, and the fraction of ethanol molecules found in the mesopore corner region remains near 2% for the entire concentration range. In contrast, the water distribution exhibits non-monotonic behavior. At C_{EtOH} = 5 g L^{-1}, about 74% of the water molecules are found in the mesopore interior. This fraction increases to 79% at C_{EtOH} = 180 g L^{-1} as water gets displaced from the micropores (decreasing from 4% to 1%) and also slightly from the mesopore surface region. At C_{EtOH} > 180 g L^{-1}, the fraction of water molecules in the mesopore interior decreases whereas those in the other three regions increase. In particular, the fraction of water adsorbed in the mesopore corner region increases from 1% to 9%.

We further analyzed the ethanol-over-water separation factor by considering micro- and mesopore regions individually (Figure 6F). At C_{EtOH} ≈ 5 g L^{-1}, the separation factor in just the SPP micropores is 400 which is about a factor of 2 lower than that in MFI-F due to water fingers extending into the SPP micropores from the mesopore region. The separation factor in the SPP micropore is about 20 times larger than the value of 18 for the entire SPP material because the larger (by volume fraction) mesopore region is barely selective for ethanol with α_{meso} = 3. At C_{EtOH} > 400 g L^{-1}, the mesopore region is actually selective for water over ethanol (with α_{meso} = 0.8 at high C_{EtOH}). The separation factor for the hydrophobic SPP micropore region is always smaller than that for MFI-F (Figure 4C) but larger than that for the mesopore region. The $\alpha_{micro}/\alpha_{meso}$ ratio diminishes from 130 at C_{EtOH}≈ 5 g L^{-1} to values near 5 for C_{EtOH} > 700 g L^{-1}.

4. CONCLUSIONS

The pillaring of MFI nanosheets with their hydrophobic micropores but hydrophilic surfaces into a house-of-cards arrangement in SPP leads to a hierarchical pore environment with very different characteristics that can be exploited for separations and catalysis. The micropore regions of SPP retain their hydrophobic character, but fingering from the pore mouth allows for limited accessibility to water. The mesopore surface with the large number of surface silanols retains its hydrophilic character, and the mesopore corners formed by the intersecting nanosheets provide an even better environment for water molecules due to the formation of hydrogen bonds with multiple silanols.

Both unary vapor-phase and binary solution-phase adsorption of water and ethanol onto hierarchical SPP are investigated in this combined molecular simulation and experimental study. From the vapor phase, ethanol preferentially adsorbs in the mesopore corners and the hydrophobic micropores. The corner sites allow for enhanced hydrogen-bond formation and stronger dispersion interactions than those on the mesopore surface, whereas the micropores allow for stronger dispersion interactions than those on any other region. The micropores are filled with ethanol before capillary condensation leads to filling of the mesopores. In contrast, unary water adsorption exhibits a different behavior. Water molecules preferentially adsorb onto the mesopore corner

https://doi.org/10.1021/acsphyschemau.1c00026
ACS Phys. Chem Au 2022, 2, 79−88

followed by the mesopore surface. Loading of water molecules in the micropores is limited to hydrogen-bonded fingers extending from the pore mouth, but percolation in the micropore does not occur even at the point where capillary condensation happens in the mesopore. For water−ethanol solutions, at low ethanol concentration, ethanol molecules are predominantly adsorbed in the micropores whereas water molecules mostly occupy the mesopores with some coadsorbed water molecules forming hydrogen bonds with ethanol molecules with the micropores. With increasing concentrations, ethanol displaces water first from the micropores then also from the mesopores. Due to the mixed-mode hydrophobic−hydrophilic character of the hierarchical SPP materials, it does not offer the same selectivity for ethanol as realized with entirely microporous MFI. The study demonstrates that, in single-unit-cell hierarchical zeolites, it is possible to segregate molecules of different polarity in distinct domains at nanometer proximity which may offer unique advantages for tandem catalysis.

■ ASSOCIATED CONTENT

Supporting Information

The Supporting Information is available free of charge at https://pubs.acs.org/doi/10.1021/acsphyschemau.1c00026.

Figures illustrating experimental adsorption/desorption cycles; description of the coadsorption approach; description of separation factors and adsorption thermodynamics; data tables (PDF)

■ AUTHOR INFORMATION

Corresponding Author

J. Ilja Siepmann − *Department of Chemistry and Chemical Theory Center, University of Minnesota, Minneapolis, Minnesota 55455-0431, United States; Department of Chemical Engineering and Materials Science, University of Minnesota, Minneapolis, Minnesota 55455-0132, United States;* orcid.org/0000-0003-2534-4507; Phone: (612) 624-1844; Email: siepmann@umn.edu; Fax: (612) 626-7541

Authors

Swagata Pahari − *Department of Chemistry and Chemical Theory Center, University of Minnesota, Minneapolis, Minnesota 55455-0431, United States*

Matheus Dorneles de Mello − *Department of Chemical Engineering and Materials Science, University of Minnesota, Minneapolis, Minnesota 55455-0132, United States;* orcid.org/0000-0002-6574-9421

Mansi S. Shah − *Department of Chemistry and Chemical Theory Center, University of Minnesota, Minneapolis, Minnesota 55455-0431, United States; Department of Chemical Engineering and Materials Science, University of Minnesota, Minneapolis, Minnesota 55455-0132, United States*

Tyler R. Josephson − *Department of Chemistry and Chemical Theory Center, University of Minnesota, Minneapolis, Minnesota 55455-0431, United States*

Limin Ren − *Department of Chemical Engineering and Materials Science, University of Minnesota, Minneapolis, Minnesota 55455-0132, United States*

Huong Giang T. Nguyen − *Facility for Adsorbent Characterization and Testing, National Institute of Standards and Technology, Gaithersburg, Maryland 20899, United States;* orcid.org/0000-0002-1052-7565

Roger D. Van Zee − *Facility for Adsorbent Characterization and Testing, National Institute of Standards and Technology, Gaithersburg, Maryland 20899, United States*

Michael Tsapatsis − *Department of Chemical Biomolecular Engineering and Institute for NanoBiotechnology, Johns Hopkins University, Baltimore, Maryland 21218, United States; Applied Physics Laboratory, Johns Hopkins University, Laurel, Maryland 20723-6099, United States;* orcid.org/0000-0001-5610-3525

Complete contact information is available at: https://pubs.acs.org/10.1021/acsphyschemau.1c00026

Author Contributions

#S.P. and M.D.d.M. contributed equally. S.P., M.S., and T.R.J. carried out and analyzed the molecular simulations. L.R. synthesized the SPP material. H.G.T.N. and R.D.v.Z. carried out the vapor-phase adsorption measurements. M.D.d.M. carried out the solution-phase measurements. M.T. and J.I.S. conceived and supervised this study. The manuscript was written by M.D.d.M. and J.I.S. with contributions from the other authors. All authors have approved the final version of the manuscript.

Notes

The authors declare no competing financial interest.

■ ACKNOWLEDGMENTS

This work is supported in part by the Catalysis Center for Energy Innovation, an Energy Frontier Research Center funded by the U.S. Department of Energy, Office of Science, Office of Basic Energy Sciences under award number DE-SC0001004 (for experimental measurements and molecular simulation of unary adsorption) and the U.S. Department of Energy, Office of Basic Energy Sciences, Division of Chemical Sciences, Geosciences and Biosciences under Award DE-FG02-17ER16362 (for molecular simulations of binary mixtures). The authors acknowledge the Minnesota Supercomputing Institute at the University of Minnesota for providing computational resources that contributed to this work. Equipment at the Facility for Adsorbent Characterization and Testing was purchased through Advanced Research Project Agency − Energy (ARPA-E) Interagency Agreement-No. 1208-0000.

■ REFERENCES

(1) Roth, W. J.; Nachtigall, P.; Morris, R. E.; Čejka, J. Two-Dimensional Zeolites: Current Status and Perspectives. *Chem. Rev.* **2014**, *114*, 4807−4837.

(2) Corma, A. Inorganic Solid Acids and Their Use in Acid-Catalyzed Hydrocarbon Reactions. *Chem. Rev.* **1995**, *95*, 559−614.

(3) Choi, M.; Na, K.; Kim, J.; Sakamoto, Y.; Terasaki, O.; Ryoo, R. Stable Single-Unit-Cell Nanosheets of Zeolite MFI as Active and Long-Lived Catalysts. *Nature* **2009**, *461*, 246−249.

(4) Saenluang, K.; Imyen, T.; Wannapakdee, W.; Suttipat, D.; Dugkhuntod, P.; Ketkaew, M.; Thivasasith, A.; Wattanakit, C. Hierarchical Nanospherical ZSM-5 Nanosheets with Uniform Al Distribution for Alkylation of Benzene with Ethanol. *ACS Appl. Nano Mater.* **2020**, *3*, 3252−3263.

(5) Peng, Y.; Lu, H.; Wang, Z.; Yan, Y. Microstructural Optimization of MFI-Type Zeolite Membranes for Ethanol-Water Separation. *J. Mater. Chem. A* **2014**, *2*, 16093−16100.

(6) Bowen, T. C.; Noble, R. D.; Falconer, J. L. Fundamentals and Applications of Pervaporation through Zeolite Membranes. *J. Membr. Sci.* **2004**, *245*, 1−33.
(7) Ackley, M. W.; Rege, S. U.; Saxena, H. Application of Natural Zeolites in the Purification and Separation of Gases. *Microporous Mesoporous Mater.* **2003**, *61*, 25−42.
(8) Delgado, J. A.; Uguina, M. A.; Sotelo, J. L.; Águeda, V. I.; García, A.; Roldán, A. Separation of Ethanol-Water Liquid Mixtures by Adsorption on Silicalite. *Chem. Eng. J.* **2012**, *180*, 137−144.
(9) Egeblad, K.; Christensen, C. H.; Kustova, M.; Christensen, C. H. Templating Mesoporous Zeolites. *Chem. Mater.* **2008**, *20*, 946−960.
(10) Christensen, C. H.; Johannsen, K.; Törnqvist, E.; Schmidt, I.; Topsøe, H.; Christensen, C. H. Mesoporous Zeolite Single Crystal Catalysts: Diffusion and Catalysis in Hierarchical Zeolites. *Catal. Today* **2007**, *128*, 117−122.
(11) Valtchev, V.; Mintova, S. Hierarchical Zeolites. *MRS Bull.* **2016**, *41*, 689−693.
(12) Chaikittisilp, W.; Suzuki, Y.; Mukti, R. R.; Suzuki, T.; Sugita, K.; Itabashi, K.; Shimojima, A.; Okubo, T. Formation of Hierarchically Organized Zeolites by Sequential Intergrowth. *Angew. Chem., Int. Ed.* **2013**, *52*, 3355−3359.
(13) Kim, J.; Choi, M.; Ryoo, R. Effect of Mesoporosity against the Deactivation of MFI Zeolite Catalyst during the Methanol-to-Hydrocarbon Conversion Process. *J. Catal.* **2010**, *269*, 219−228.
(14) Fan, W.; Snyder, M. A.; Kumar, S.; Lee, P. S.; Yoo, W. C.; McCormick, A. V.; Lee Penn, R.; Stein, A.; Tsapatsis, M. Hierarchical Nanofabrication of Microporous Crystals with Ordered Mesoporosity. *Nat. Mater.* **2008**, *7*, 984−991.
(15) Liu, J.; Yang, X.; Wang, C.; Ye, L.; Sun, H. Synthesis of Hierarchical 5A Zeolites to Improve the Separation Efficiency of N-Paraffins. *Adsorpt. Sci. Technol.* **2019**, *37*, 530−544.
(16) Dabbawala, A. A.; Ismail, I.; Vaithilingam, B. V.; Polychronopoulou, K.; Singaravel, G.; Morin, S.; Berthod, M.; Al Wahedi, Y. Synthesis of Hierarchical Porous Zeolite-Y for Enhanced CO2 Capture. *Microporous Mesoporous Mater.* **2020**, *303*, 110261.
(17) Na, K.; Choi, M.; Park, W.; Sakamoto, Y.; Terasaki, O.; Ryoo, R. Pillared MFI Zeolite Nanosheets of a Single-Unit-Cell Thickness. *J. Am. Chem. Soc.* **2010**, *132*, 4169−4177.
(18) Liu, D.; Bhan, A.; Tsapatsis, M.; Al Hashimi, S. Catalytic Behavior of Brønsted Acid Sites in MWW and MFI Zeolites with Dual Meso- and Microporosity. *ACS Catal.* **2011**, *1*, 7−17.
(19) Zhang, X.; Liu, D.; Xu, D.; Asahina, S.; Cychosz, K. A.; Agrawal, K. V.; Wahedi, Y. Al; Bhan, A.; Hashimi, S. Al; Terasaki, O.; Thommes, M.; Tsapatsis, M. Synthesis of Self-Pillared Zeolite Nanosheets by Repetitive Branching. *Science* **2012**, *336*, 1684−1687.
(20) Ren, L.; Guo, Q.; Kumar, P.; Orazov, M.; Xu, D.; Alhassan, S. M.; Mkhoyan, K. A.; Davis, M. E.; Tsapatsis, M. Self-Pillared, Single-Unit-Cell Sn-MFI Zeolite Nanosheets and Their Use for Glucose and Lactose Isomerization. *Angew. Chem., Int. Ed.* **2015**, *54*, 10848−10851.
(21) Abdelrahman, O. A.; Park, D. S.; Vinter, K. P.; Spanjers, C. S.; Ren, L.; Cho, H. J.; Zhang, K.; Fan, W.; Tsapatsis, M.; Dauenhauer, P. J. Renewable Isoprene by Sequential Hydrogenation of Itaconic Acid and Dehydra-Decyclization of 3-Methyl-Tetrahydrofuran. *ACS Catal.* **2017**, *7*, 1428−1431.
(22) Xu, D.; Abdelrahman, O.; Ahn, S. H.; Guefrachi, Y.; Kuznetsov, A.; Ren, L.; Hwang, S.; Khaleel, M.; Al Hassan, S.; Liu, D.; Hong, S. B.; Dauenhauer, P.; Tsapatsis, M. A Quantitative Study of the Structure−Activity Relationship in Hierarchical Zeolites Using Liquid-Phase Reactions. *AIChE J.* **2019**, *65*, 1067−1075.
(23) Josephson, T. R.; Dejaco, R. F.; Pahari, S.; Ren, L.; Guo, Q.; Tsapatsis, M.; Siepmann, J. I.; Vlachos, D. G.; Caratzoulas, S. Cooperative Catalysis by Surface Lewis Acid/Silanol for Selective Fructose Etherification on Sn-SPP Zeolite. *ACS Catal.* **2018**, *8*, 9056−9065.
(24) Josephson, T. R.; Dauenhauer, P. J.; Tsapatsis, M.; Siepmann, J. I. Adsorption of Furan, Hexanoic Acid, and Alkanes in a Hierarchical Zeolite at Reaction Conditions: Insights from Molecular Simulations. *J. Comput. Sci.* **2021**, *48*, 101267.
(25) Bregante, D. T.; Flaherty, D. W. Impact of Specific Interactions among Reactive Surface Intermediates and Confined Water on Epoxidation Catalysis and Adsorption in Lewis Acid Zeolites. *ACS Catal.* **2019**, *9*, 10951−10962.
(26) Mei, D.; Lercher, J. A. Effects of Local Water Concentrations on Cyclohexanol Dehydration in H-BEA Zeolites. *J. Phys. Chem. C* **2019**, *123*, 25255−25266.
(27) Sievers, C.; Scott, S. L.; Noda, Y.; Qi, L.; Albuquerque, E. M.; Rioux, R. M. Phenomena Affecting Catalytic Reactions at Solid-Liquid Interfaces. *ACS Catal.* **2016**, *6*, 8286−8307.
(28) Mallon, E. E.; Jeon, M. Y.; Navarro, M.; Bhan, A.; Tsapatsis, M. Probing the Relationship between Silicalite-1 Defects and Polyol Adsorption Properties. *Langmuir* **2013**, *29*, 6546−6555.
(29) DeJaco, R. F.; Dorneles de Mello, M.; Nguyen, H. G. T.; Jeon, M. Y.; van Zee, R. D.; Tsapatsis, M.; Siepmann, J. I. Vapor and Liquid Phase Adsorption of Alcohol and Water in Silicalite□1 Synthesized in Fluoride Media. *AIChE J.* **2020**, *66*, e16868.
(30) van Koningsveld, H.; Van Bekkum, H.; Jansen, J. C. On the Location and Disorder of the Tetrapropylammonium (TPA) Ion in Zeolite ZSM□5 with Improved Framework Accuracy. *Acta Crystallogr., Sect. B: Struct. Sci.* **1987**, *43*, 127−132.
(31) Bai, P.; Olson, D. H.; Tsapatsis, M.; Siepmann, J. I. Understanding the Unusual Adsorption Behavior in Hierarchical Zeolite Nanosheets. *ChemPhysChem* **2014**, *15*, 2225−2229.
(32) Lopez-Orozco, S.; Inayat, A.; Schwab, A.; Selvam, T.; Schwieger, W. Zeolitic Materials with Hierarchical Porous Structures. *Adv. Mater.* **2011**, *23*, 2602−2615.
(33) Jorgensen, W. L.; Chandrasekhar, J.; Madura, J. D.; Impey, R. W.; Klein, M. L. Comparison of Simple Potential Functions for Simulating Liquid Water. *J. Chem. Phys.* **1983**, *79*, 926−935.
(34) Martin, M. G.; Siepmann, J. I. Transferable Potentials for Phase Equilibria. 1. United-Atom Description of n-Alkanes. *J. Phys. Chem. B* **1998**, *102*, 2569−2577.
(35) Chen, B.; Potoff, J. J.; Siepmann, J. I. Monte Carlo Calculations for Alcohols and Their Mixtures with Alkanes. Transferable Potentials for Phase Equilibria. 5. United-Atom Description of Primary, Secondary, and Tertiary Alcohols. *J. Phys. Chem. B* **2001**, *105*, 3093−3104.
(36) Bai, P.; Tsapatsis, M.; Siepmann, J. I. TraPPE-Zeo: Transferable Potentials for Phase Equilibria Force Field for All-Silica Zeolites. *J. Phys. Chem. C* **2013**, *117*, 24375−24387.
(37) Rafferty, J. L.; Siepmann, J. I.; Schure, M. R. Influence of Bonded-Phase Coverage in Reversed-Phase Liquid Chromatography via Molecular Simulation. I. Effects on Chain Conformation and Interfacial Properties. *J. Chromatogr. A* **2008**, *1204*, 11−19.
(38) Allen, M. P.; Tildesley, D. J. *Computer Simulation of Liquids*; Oxford University Press: Oxford, 1987.
(39) Vlugt, T. J. H.; Martin, M. G.; Smit, B.; Siepmann, J. I.; Krishna, R. Improving the Efficiency of the Configurational-Bias Monte Carlo Algorithm. *Mol. Phys.* **1998**, *94*, 727−733.
(40) Martin, M. G.; Siepmann, J. I. Novel Configurational-Bias Monte Carlo Method for Branched Molecules. Transferable Potentials for Phase Equilibria. 2. United-Atom Description of Branched Alkanes. *J. Phys. Chem. B* **1999**, *103*, 4508−4517.
(41) Panagiotopoulos, A. Z.; Quirke, N.; Stapleton, M.; Tildesley, D. J. Phase Equilibria by Simulation in the Gibbs Ensemble Alternative Derivation, Generalization and Application to Mixture and Membrane Equilibria. *Mol. Phys.* **1988**, *63*, 527−545.
(42) Smit, B.; De Smedt, P.; Frenkel, D. Computer Simulations in the Gibbs Ensemble. *Mol. Phys.* **1989**, *68* (4), 931−950.
(43) Ramachandran, C. E.; Chempath, S.; Broadbelt, L. J.; Snurr, R. Q. Water Adsorption in Hydrophobic Nanopores: Monte Carlo Simulations of Water in Silicalite. *Microporous Mesoporous Mater.* **2006**, *90*, 293−298.
(44) Trzpit, M.; Soulard, M.; Patarin, J.; Desbiens, N.; Cailliez, F.; Boutin, A.; Demachy, I.; Fuchs, A. H. The Effect of Local Defects on Water Adsorption in Silicalite-1 Zeolite: A Joint Experimental and Molecular Simulation Study. *Langmuir* **2007**, *23*, 10131−10139.

https://doi.org/10.1021/acsphyschemau.1c00026
ACS Phys. Chem Au 2022, 2, 79−88

(45) Castillo, J. M.; Silvestre-Albero, J.; Rodriguez-Reinoso, F.; Vlugt, T. J. H.; Calero, S. Water Adsorption in Hydrophilic Zeolites: Experiment and Simulation. *Phys. Chem. Chem. Phys.* **2013**, *15*, 17374−17382.
(46) Zhang, K.; Lively, R. P.; Noel, J. D.; Dose, M. E.; McCool, B. A.; Chance, R. R.; Koros, W. J. Adsorption of Water and Ethanol in MFI-Type Zeolites. *Langmuir* **2012**, *28*, 8664−8673.
(47) Cheng, C. H.; Bae, T. H.; McCool, B. A.; Chance, R. R.; Nair, S.; Jones, C. W. Postsynthesis Organic Functionalization of the Internal Surface of Zeolite MFI. *J. Phys. Chem. C* **2008**, *112*, 3543−3551.
(48) Bai, P.; Tsapatsis, M.; Siepmann, J. I. Multicomponent Adsorption of Alcohols onto Silicalite-1 from Aqueous Solution: Isotherms, Structural Analysis, and Assessment of Ideal Adsorbed Solution Theory. *Langmuir* **2012**, *28*, 15566−15576.
(49) Bai, P.; Jeon, M. Y.; Ren, L.; Knight, C.; Deem, M. W.; Tsapatsis, M.; Siepmann, J. I. Discovery of Optimal Zeolites for Challenging Separations and Chemical Transformations Using Predictive Materials Modeling. *Nat. Commun.* **2015**, *6*, 5912.
(50) Dejaco, R. F.; Elyassi, B.; Dorneles De Mello, M.; Mittal, N.; Tsapatsis, M.; Siepmann, J. I. Understanding the Unique Sorption of Alkane- α, ω -Diols in Silicalite-1. *J. Chem. Phys.* **2018**, *149*, 072331.
(51) Zhou, H.; Mouzon, J.; Farzaneh, A.; Antzutkin, O. N.; Grahn, M.; Hedlund, J. Colloidal Defect-Free Silicalite-1 Single Crystals: Preparation, Structure Characterization, Adsorption, and Separation Properties for Alcohol/Water Mixtures. *Langmuir* **2015**, *31*, 8488−8494.
(52) Ueno, K.; Yamada, S.; Watanabe, T.; Negishi, H.; Okuno, T.; Tawarayama, H.; Ishikawa, S.; Miyamoto, M.; Uemiya, S.; Oumi, Y. Hydrophobic *BEA-Type Zeolite Membranes on Tubular Silica Supports for Alcohol/Water Separation by Pervaporation. *Membranes (Basel, Switz.)* **2019**, *9*, 86.
(53) Weitkamp, J.; Ernst, S.; Günzel, B.; Deckwer, W. D. Separation of Gaseous Water/Ethanol Mixtures by Adsorption on Hydrophobic Zeolites. *Zeolites* **1991**, *11*, 314−317.
(54) Weyd, M.; Richter, H.; Puhlfürß, P.; Voigt, I.; Hamel, C.; Seidel-Morgenstern, A. Transport of Binary Water-Ethanol Mixtures through a Multilayer Hydrophobic Zeolite Membrane. *J. Membr. Sci.* **2008**, *307* (2), 239−248.
(55) Farzaneh, A.; Zhou, M.; Potapova, E.; Bacsik, Z.; Ohlin, L.; Holmgren, A.; Hedlund, J.; Grahn, M. Adsorption of Water and Butanol in Silicalite-1 Film Studied with in Situ Attenuated Total Reflectance-Fourier Transform Infrared Spectroscopy. *Langmuir* **2015**, *31*, 4887−4894.
(56) Ben-Naim, A. *Statistical Thermodynamics for Chemists and Biochemists*; Plenum: New York, 1992.
(57) Ben-Naim, A.; Mazo, R. Size Dependence of Solvation Gibbs Energies: A Critique and a Rebuttal of Some Recent Publications. *J. Phys. Chem. B* **1997**, *101*, 11221−11225.

https://doi.org/10.1021/acsphyschemau.1c00026
ACS Phys. Chem Au 2022, 2, 79−88